Atmospheric
Measurement
Techniques

# High-spatial-resolution mapping of precipitable water vapour using SAR interferograms, GPS observations and ERA-Interim reanalysis

**Wei Tang[1], Mingsheng Liao[1,2], Lu Zhang[1], Wei Li[3], and Weimin Yu[4]**

[1]State Key Laboratory of Information Engineering in Surveying, Mapping and Remote Sensing,
Wuhan University, Wuhan, China
[2]Collaborative Innovation Center for Geospatial Technology, Wuhan University, Wuhan, China
[3]Shanghai Academy of Spaceflight Technology, Shanghai, China
[4]Shanghai Institute of Satellite Engineering, Shanghai, China

*Correspondence to:* Lu Zhang (luzhang@whu.edu.cn)

**Abstract.** A high spatial and temporal resolution of the precipitable water vapour (PWV) in the atmosphere is a key requirement for the short-scale weather forecasting and climate research. The aim of this work is to derive temporally differenced maps of the spatial distribution of PWV by analysing the tropospheric delay "noise" in interferometric synthetic aperture radar (InSAR). Time series maps of differential PWV were obtained by processing a set of EN-VISAT ASAR (Advanced Synthetic Aperture Radar) images covering the area of southern California, USA from 6 October 2007 to 29 November 2008. To get a more accurate PWV, the component of hydrostatic delay was calculated and subtracted by using ERA-Interim reanalysis products. In addition, the ERA-Interim was used to compute the conversion factors required to convert the zenith wet delay to water vapour. The InSAR-derived differential PWV maps were calibrated by means of the GPS PWV measurements over the study area. We validated our results against the measurements of PWV derived from the Medium Resolution Imaging Spectrometer (MERIS) which was located together with the ASAR sensor on board the ENVISAT satellite. Our comparative results show strong spatial correlations between the two data sets. The difference maps have Gaussian distributions with mean values close to zero and standard deviations below 2 mm. The advantage of the InSAR technique is that it provides water vapour distribution with a spatial resolution as fine as 20 m and an accuracy of $\sim 2$ mm. Such high-spatial-resolution maps of PWV could lead to much greater accuracy in meteorological understanding and quantitative

precipitation forecasts. With the launch of Sentinel-1A and Sentinel-1B satellites, every few days (6 days) new SAR images can be acquired with a wide swath up to 250 km, enabling a unique operational service for InSAR-based water vapour maps with unprecedented spatial and temporal resolution.

## 1 Introduction

The performance of interferometric synthetic aperture radar (InSAR) data when deriving digital elevation models (DEMs) or precisely measuring surface deformation of the Earth is limited by the tropospheric delay mainly caused by the water vapour content in the lower part ($\leq 1.5$ km) of the troposphere (Beauducel et al., 2000; Liao et al., 2013; Zebker et al., 1997). Although the water vapour contributes to only about 10 % of total atmospheric delay, this source of error is not easily eliminated due to its high spatial and temporal variability. Our aim in this paper is to investigate the tropospheric delay "noise" of InSAR as a meteorological signal to measure the water vapour content in the atmosphere. We will present a new approach for accurate water vapour estimation with a high spatial resolution by combing InSAR observations, GPS data and a global atmospheric model (ERA-Interim), and we will assess its performance.

Various techniques have been applied to measure the horizontal and vertical distributions of water vapour in the atmosphere either from space or the ground. Water vapour

measurements produced by radiosondes or water vapour radiometers are limited in the spatial and temporal resolution. Global navigation satellite systems (GNSS) provide water vapour measurements with a dense temporal sampling and high accuracy but the GNSS networks are too sparse and irregular to capture fine-scale water vapour fluctuations. Passive multispectral imagers such as the Medium Resolution Imaging Spectrometer (MERIS) and Moderate Resolution Imaging Spectroradiometer (MODIS) only produce continuous water vapour maps during daytime or under cloud-free weather conditions. These limitations are the main error source in short-term (0–24 h) precipitation prediction. The advantage of satellite-based InSAR, a relatively new tool for measuring water vapour content, is that it could provide maps of water vapour with a spatial resolution as fine as 10–20 m over a swath of ground about 100 km wide.

With the new launch of Sentinel-1A satellite (launched in April 2014), we can get SAR data with a repeat acquisition rate of 12 days and, in combination with the recently launched (April 2016) Sentinel-1B, the acquisition rate decreases to 6 days. This high repeat rate together with the large illuminated swath (250 km) make the Sentinel 1 constellation a more attractive source of data for meteorology studies.

In this paper, we use the InSAR data in combination with GPS measurements and ERA-Interim reanalysis products to precisely estimate the water vapour content in the atmosphere. The main concept of InSAR for constructing water vapour maps is that the tropospheric phase delay is considered the signal of interest to be extracted and the other phase components are treated as noise to be removed. The tropospheric phase delay mainly consists of two components: hydrostatic delay and wet delay. The hydrostatic delay varies with local temperature and atmospheric pressure, smoothly in time and space, while the wet delay varies with water vapour partial pressure, which is more spatially and temporally varying. Within a typical interferogram area of 100 km × 100 km, the pressure usually varies less than 1 hPa, while significant changes of the water vapour partial pressure are common. Consequently, the wet delay variability in the interferogram is much greater than the hydrostatic delay. Therefore, most studies have focused on estimating the wet delay and neglected the hydrostatic delay. However, recent studies also show that hydrostatic delay varies significantly at low elevation and cannot be neglected (Doin et al., 2009; Jolivet et al., 2014). Thus, to obtain accurate PWV maps, hydrostatic delay in InSAR must be taken into account. In this work, we compute the component of hydrostatic delay by using ERA-Interim reanalysis products. Using the water vapour conversion factor, the InSAR-derived zenith wet delay is then mapped onto precipitable water vapour (PWV), a quantity representing the water vapour content in the atmosphere. In this study, the outputs of temperature and specific humidity from the ERA-Interim model are used to estimate this water vapour conversion factor. It should be noted that water vapour maps from InSAR are derived from the differ-

ence between the water vapour present at the time of the synthetic aperture radar (SAR) overpass, with a temporal separation of one or more days, which we call Δ PWV hereafter. The temporal interval depends on the space-borne InSAR mission: 1 day (tandem ERS-1/2), 11 days (TerraSAR-X, Cosmo-SkyMed), 12 days (Sentinel-1), 35 days (ENVISAT ASAR, RADARSAT) and 46 days (ALOS-PALSAR). The main problem is that the Δ PWV differential maps from InSAR suffer from an unknown bias, which requires a reference observation to calibrate each Δ PWV map. The calibration procedure was implemented by using absolute measurements of PWV from a few GPS stations in our study area. After that, the calibrated Δ PWV maps were evaluated by being compared to the Δ PWV from the collocated GPS stations. Finally, we made a comparative analysis of Δ PWV maps from InSAR and MERIS pixel by pixel, and by inspecting the spatial properties.

## 2 Study area and data sets

We carried out the study using data sets collected in the Los Angeles basin, located in southern California, USA. This study area neighbours the Pacific Ocean in the west and south-west, thus is rich with atmospheric water vapour and is well covered by a dense network of continuous GPS receivers. These conditions make it particularly suitable for atmospheric water vapour studies. Figure 1 shows the topography map of the study area. A set of $N = 8$ ENVISAT ASAR SLC (Advanced Synthetic Aperture Radar Single Look Complex) images were acquired over this region for the period between 6 October 2007 to 29 November 2008. The image was acquired during descending passes, Track 170, with the average look angle $\theta = 22.6°$. Actually, the value of look angle $\theta$ varies over the SAR scene from near range to far range between 16.5 and 23.2°. Accuracy may improve if local look angle of every pixels within interferogram is considered when calculating the mapping function. We used the average look angle in our study. The acquisition time was 18:01 UTC. For SAR interferometric processing, an external DEM with 30 m height postings from Shuttle Radar Topography Mission (SRTM) (Farr et al., 2007) was used for removing the influence of topography and the Earth's curvature, while the precise orbit information from Delft Institute for Earth-Oriented Space Research was utilized for minimizing the orbital errors. The black square in Fig. 1 shows the footprint of SAR images.

We used 29 permanent GPS stations in the Southern California Integrated GPS Network (SCIGN) within the SAR image scene to estimate atmospheric water vapour over southern California. SCIGN is one of the densest GPS network in the world, with more than 250 continuously operated GPS stations. Most of the GPS stations of SCIGN have been integrated into the Plate Boundary Observatory (PBO) in 2008. PBO has two GPS Analysis Centers (ACs) that process raw
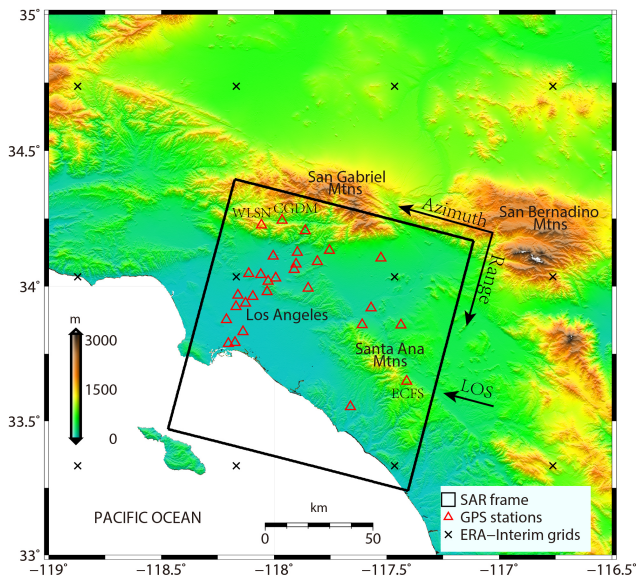
**Figure 1.** The topography map of the study area. The red triangles represent the locations of GPS stations. The locations of GPS stations CGDM, ECFS and WLSN are indicated. The black box defines the area of ENVISAT ASAR images. Black crosses indicate the position of the ERA-Interim model grid nodes used in this study. The arrow on the right side of the SAR frame indicates the line of sight (LOS) of the radar signal.

GPS data and produce position solutions for stations in the PBO network as well as other selected stations. One AC is operated by the Geodesy Laboratory at Central Washington University (CWU) and uses the GIPSY/OASIS-II processing package. The other AC is located at the New Mexico Institute of Technology (NMT) and uses GAMIT/GLOBK. The Analysis Centres provide tropospheric data products, including zenith atmospheric delay, that are archived at the UNAVCO Data Center and are openly and freely available (http://www.unavco.org/data/data.html). The availability of GPS measurements also allowed us to separate possible surface deformation from the atmospheric signals in differential interferograms. The red triangles in Fig. 1 represent the locations of GPS stations.

The ERA-Interim reanalysis from the European Centre for Medium-Range Weather Forecasts (ECMWF) is used to produce maps of hydrostatic delay and water vapour conversion factor. ERA-Interim is a global atmospheric model which was conceived to address some of the problems seen in ERA-40 (Dee et al., 2011). It is based on 4-dimensional variational assimilation of global surface and satellite meteorological data. The outputs of ERA-Interim used in our study are estimates of temperature, specific humidity and geopotential height, defined at 37 pressure levels (1000–1 hPa), and a spatial resolution of 0.75° (∼ 75 km). The black crosses in Fig. 1 show the distribution of ERA-Interim model grid nodes used in this study. The MERIS is located together with

the ASAR sensor on board the ENVISAT satellite (Bennartz and Fischer, 2001), thus the simultaneous water vapour measurements from MERIS were used as a reference data for comparison and evaluation.

## 3 Estimating PWV from InSAR

Here, we present the methods for obtaining zenith wet delay from SAR interferogram and converting it to PWV. In Sect. 3.1, the retrieval of zenith wet delay from the SAR interferogram is described. Section 3.2 describes the method for computing the conversion factor required to map the zenith wet delay onto PWV by using ERA-Interim reanalysis. In Sect. 3.3, the approach for calibrating the PWV estimated from InSAR using GPS observations is discussed.

### 3.1 Atmospheric delay in InSAR

The unwrapped interferometric phase for each pixel in an interferogram is given by the superposition of several components including topography, Earth surface displacement and atmosphere. It can be written as follows:

$$\varnothing_{\mathrm{int}} = \varnothing_{\mathrm{topo}} + \varnothing_{\mathrm{defo}} + \varnothing_{\mathrm{orb}} + \varnothing_{\mathrm{atm}} + \varnothing_{\mathrm{noise}}, \tag{1}$$

where $\varnothing_{\mathrm{topo}}$ is the phase contribution from land topography, $\varnothing_{\mathrm{defo}}$ represents the ground deformation between the acquisitions, $\varnothing_{\mathrm{orb}}$ counts for the phase caused by inaccurate satellite orbit, $\varnothing_{\mathrm{atm}}$ indicates the atmospheric state variations during SAR acquisitions and $\varnothing_{\mathrm{noise}}$ denotes the noise component including system thermal noise, decorrelation noise, co-registration noise and processing noise. The contribution of topography is compensated for by using an external DEM (the 30 m SRTM DEM is used in this study, Fig. 2a). An example of an original unwrapped interferogram (master image from 16 August 2008, slave image from 25 October 2008) is shown in Fig. 2b, with the topographic phase component subtracted. The orbital error was modelled by a network deramping method described in Jolivet et al. (2011) and estimated separately from the unwrapped phase. A strong, localized, vertical displacement in the Los Angeles basin area was observed in a number of interferograms, although those interferograms possess short temporal baselines. The rapidly subsiding displacement area in the Los Angeles basin region was masked out from all interferograms to avoid mixing the atmospheric signal with surface deformation. After subtracting the topographic phase and orbital ramp, the residual phase in the unwrapped interferograms only results from the atmospheric delay, which can be split into hydrostatic, wet, liquid and ionospheric components. In this study, we only focus on the hydrostatic and wet components in the troposphere, as the delay induced by liquid water is expected to be small under usual conditions, and the ionospheric components are assumed to be small for the C-band SAR signal (Hanssen, 2001). Thus, it leads to the tropospheric phase delay $\varnothing_{\mathrm{trop}}$ as
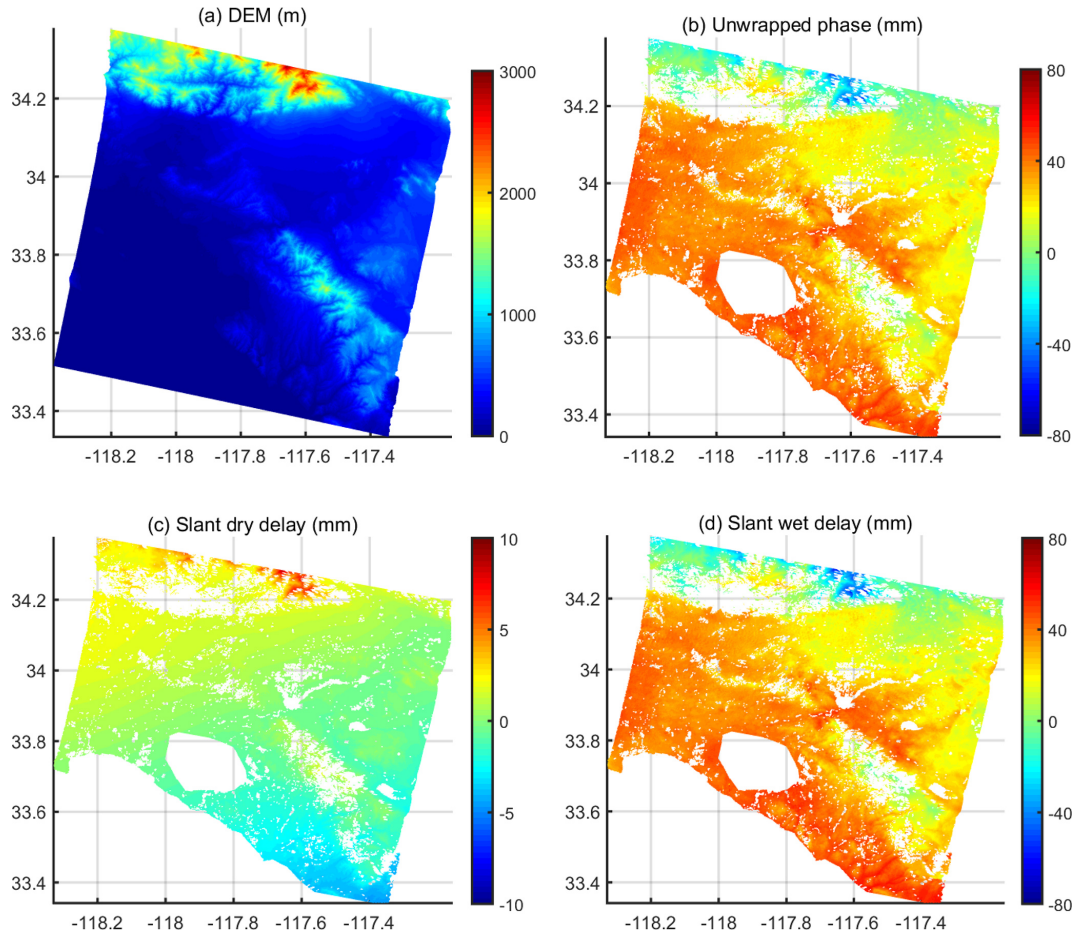
**Figure 2. (a)** Regional land topography from SRTM at interferogram pixels. **(b)** Unwrapped phase of differential interferogram (master image from 16 August 2008, slave image from 25 October 2008). **(c)** Slant hydrostatic delay difference maps predicted from the ERA-Interim model. **(d)** Slant wet delay difference obtained by subtracting **(c)** from **(b)**. The rapidly subsiding areas are masked out in **(b)**, **(c)** and **(d)**.

(Doin et al., 2009)

$$\varnothing_{\mathrm{trop}} = \varnothing_{\mathrm{hyd}} + \varnothing_{\mathrm{wet}}, \tag{2}$$

where

$$\varnothing_{\mathrm{hyd}}(z) = -\frac{4\pi}{\lambda \cos\theta_{\mathrm{inc}}} 10^{-6} \left[\frac{k_1 R_d}{g_0}\left(P(z) - P(z_0)\right)\right] \tag{3}$$

$$\varnothing_{\mathrm{wet}}(z) = -\frac{4\pi}{\lambda \cos\theta_{\mathrm{inc}}} 10^{-6} \int\limits_{z}^{z_{\mathrm{ref}}}$$
$$\left[\left(k_2 - \frac{R_d}{R_v}k_1\right)\frac{e(z)}{T(z)} + k_3\frac{e(z)}{T(z)^2}\right]\mathrm{d}z. \tag{4}$$

The hydrostatic delay $\varnothing_{\mathrm{hyd}}$ is calculated using the specific gas constant for hydrostatic air $R_d$, the local gravity $g_0$ at the mass centre of the atmospheric column between $z$ and $z_{\mathrm{ref}}$ and air pressure $P$. The wet delay $\varnothing_{\mathrm{wet}}$ is computed using the partial pressure of water vapour $e$, water vapour specific gas

constant $R_v$ and temperature $T$. $z_{\mathrm{ref}}$ represents a reference height (30 km used in this study) above which the delay is assumed to be nearly unchanged with time. The atmospheric refractivity constants $k_1$, $k_2$ and $k_3$ are determined in Smith and Weintraub (1953) and $\left(k_2 - \frac{R_d}{R_v}k_1\right)$ is often named $k_2' = 0.233 \,\mathrm{K\,Pa}^{-1}$. $\lambda$ is the radar wavelength and $-\frac{4\pi}{\lambda}$ is a scale factor to convert the delay in millimetre into phase in radian. $\theta_{\mathrm{inc}}$ is the radar incidence angle and the factor $\frac{1}{\cos(\theta_{\mathrm{inc}})}$ is a mapping function applied to project the delay from the zenith direction to the radar line of sight (LOS). The constants in Eqs. (3) and (4) are listed in Table 2.

The hydrostatic component of tropospheric delay depends on variations in atmospheric pressure. This pressure at a given altitude changes over time, even if slightly, up to a few percent of the total pressure, thus resulting in a difference of hydrostatic delay to a few centimetres. Moreover, the changes of terrain height introduce a spatial gradient in the atmospheric pressure across the SAR scene, which re-
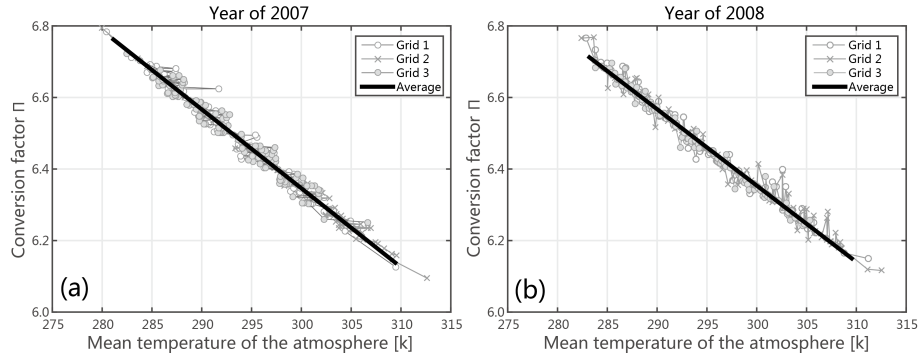
**Figure 3.** Conversion factor $\Pi$ estimated based on the water vapour partial pressure and temperature extracted at three ERA-Interim model grids located within the SAR scene (see Fig. 1). The black line is the linear regression between the averaged conversion factors and the mean temperature. The measurements were taken at 18:00 UTC (close to the SAR acquisition time of 18:01 UTC, making the time difference between these two data sets negligible) over 120 days (10 days/month) in the years 2007 **(a)** and 2008 **(b)**.

sults in a spatially variable signal in the hydrostatic delay (Mateus et al., 2013b). The variation of hydrostatic delay depending on the topography could be up to 15 mm in our study area. Therefore, in order to accurately derive the wet delay, the hydrostatic delay must be precisely estimated and subtracted from the total tropospheric delay. This delay can be calculated if the atmospheric pressure is known along the signal propagation path or along the zenith direction. In this work, we used the vertical profiles of atmospheric pressure provided by ERA-Interim reanalysis products to predict this component of hydrostatic delay. We interpolated the atmospheric pressure onto altitude profiles on each ERA-Interim model grid using a spline interpolation and calculated the hydrostatic delay using Eq. (3). The resulting vertical profiles of hydrostatic delay were horizontally interpolated to the resolution of SAR interferogram using a bilinear interpolation. We also used the outputs of temperature and relative humidity from the ERA-Interim model to produce the maps of water vapour conversion factor using the same interpolation strategy; this will be discussed in next subsection. The map of hydrostatic delay is displayed in Fig. 2c. This delay represents a long-wavelength signal, is smooth in space and rose up to 1 cm on the mountain areas. The slant wet delay (Fig. 2d) was obtained by subtracting the hydrostatic delay from the total tropospheric delay. The slant wet delay difference in LOS was converted to the zenith wet delay difference ($\Delta$ZWD) in millimetres using a simple mapping function:

$$\Delta \text{ZWD}_{\text{InSAR}} = -\frac{\lambda \cos \theta_{\text{inc}}}{4\pi} \varnothing_{\text{wet}}. \tag{5}$$

### 3.2 Conversion of ZWD into PWV

The zenith wet delay is considered to be a measurement of the water vapour content in the atmosphere. The relationship between the ZWD and PWV can be expressed as follows (Bevis et al., 1994):

$$\text{PWV} = \kappa \times \text{ZWD} \quad \text{or} \quad \text{ZWD} = \Pi \times \text{PWV}, \tag{6}$$

where $\kappa$ is the water vapour conversion factor and $\Pi = \kappa^{-1}$ is calculated by the following equation:

$$\Pi = 10^{-6} \rho R_{\text{v}} \left( \frac{k_3}{T_{\text{m}}} + k_2 - \frac{R_d}{R_{\text{v}}} k_1 \right), \tag{7}$$

where $\rho$ is the density of the liquid water (listed in Table 2). $T_{\text{m}}$ is the weighted mean temperature of the atmosphere and is related to the surface temperature $T_{\text{s}}$ in degrees Kelvin (Bevis et al., 1992).

$$T_{\text{m}} \approx 70.2 + 0.72 \times T_{\text{s}} \tag{8}$$

Using this relationship to estimate $T_{\text{m}}$ will produce approximately 2 % error in PWV (Bevis et al., 1992). The most accurate way to compute the mean temperature is to calculate the following integral equation between the ground surface $z_0$ and the reference height $z_{\text{ref}}$, given by (Davis et al., 1985)

$$T_{\text{m}} = \frac{\int_{z_0}^{z_{\text{ref}}} \left( \frac{e}{T} \right) \mathrm{d}z}{\int_{z_0}^{z_{\text{ref}}} \left( \frac{e}{T^2} \right) \mathrm{d}z}. \tag{9}$$

The value of $\Pi$ is dimensionless and usually ranges from 6.0 to 6.5 (and could be up to 7.0 in some circumstances) (Bevis et al., 1992). For the purpose of rough conversion between ZWD and PWV, an empirical constant $\Pi = 6.25$ ($\kappa = 0.16$) was used. However, the actual value of $\kappa$ changes with water vapour pressure and temperature, then minor errors in $\kappa$ could result in significant biases in PWV. For example, using the constant value $\kappa = 0.16$ and assuming a ZWD of 200 mm, the corresponding value of PWV is 32 mm. However, if the value of $\kappa$ is computed using Eqs. (7) and (9) as 0.15, then the value of PWV will be 30 mm. In fact, the larger the ZWD, the more critical the value of $\kappa$. Rather than using the empirical constant value, we evaluated the conversion factor $\kappa$ at each pixel of the SAR interferogram using ERA-Interim reanalysis. To compute the weighted mean temperature $T_{\text{m}}$, the outputs of ERA-Interim we used are the vertical

profiles of temperature and relative humidity. The relative humidity is converted to partial pressure of water vapour $e$ by a mixed Clausius–Clapeyron equation (Jolivet et al., 2011). To evaluate the sensitivity of $\Pi$ to the weighted mean temperature $T_m$, its values are computed over 120 days (10 days in one month) in the years 2007 and 2008. Figure 3 plots $\Pi$ against the average $T_m$ for the three ERA-Interim model grids (indicated as the black crosses in Fig. 1) located within the SAR scene. From Fig. 3, we observed that the value of $\Pi$ changes with $T_m$, and $\Pi$ is in the range of 6.09 to 6.79 in the year of 2007 (Fig. 3a), whereas it varies between 6.17 and 6.74 in the year of 2008 (Fig. 3b). The fitted average curves linearly decrease with rates of $-0.0214$ and $-0.0221/\mathrm{K}$ respectively. As expected the value of $\Pi$ is much higher on winter days (low temperature) than summer days (high temperature). On the other hand, since the temperature generally decreases with altitude in the troposphere, the conversion factor is correlated with the elevation. Therefore, using the empirical value of $\kappa = 0.16$ is not appropriate for the whole study area; rather its value is calculated using global atmospheric model ERA-Interim. Figure 4 shows the spatial distribution map of $\Pi$ on 16 August 2008 produced by ERA-Interim. It can be seen that the value of $\Pi$ varies spatially and it has a higher value on the mountainous areas than those areas with a flat terrain. We then averaged the spatial maps of $\Pi$ at the two interferometric acquisition times to derive the conversion factors for mapping the wet delay onto water vapour.

## 3.3   InSAR PWV calibrated by GPS PWV

PWV estimated from GPS is not directly comparable with $\Delta$ PWV estimated from InSAR. The unwrapping procedure introduces an arbitrary constant in the unwrapped phase, so the InSAR technique can just measure the $\Delta$ PWV with an unknown bias, whereas the GPS-based $\Delta$ PWV is unbiased. To resolve this problem, $\Delta$ PWV maps derived from InSAR are calibrated by GPS-based $\Delta$ PWV. It should be noted that only the signals from satellites with elevation angle larger than the cut-off elevation angle are recorded by the GPS receiver. Thus, the PWV estimates from GPS are derived by being weighted with the elevation and azimuth angles of the individual ray paths from the GPS satellites to the receiver. Figure 5 shows the schematic diagram of this effect. The cut-off elevation angle is set to 15° and assumes the water vapour is concentrated in the lower part (1.4 km) of the troposphere; the corresponding cone radius is approximately 5.4 km. All observations outside this cone are discarded. We averaged the $\Delta$ PWV values of the interferogram pixels located within the corresponding circular area before comparing InSAR measurements to that of GPS. We calculated the temporal difference of the PWV at each GPS station, at about the same acquisition time as the two interferometric SAR images. The InSAR $\Delta$ PWV calibration process is to determine the constant $K$ by minimizing the following cost function (Mateus
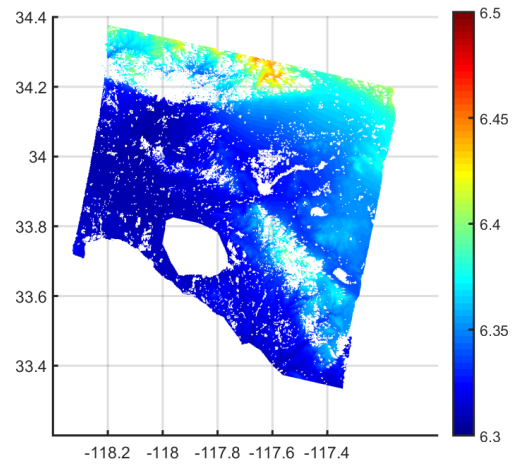


**Figure 4.** The spatial distribution of conversion factor $\Pi$ calculated based on ERA-Interim. It is calculated at the time 18:00 UTC on 16 August 2008.

et al., 2013a).

$$\sum_{k=1}^{N_{\mathrm{GPS}}} \left\{ \Delta\mathrm{PWV}_k^{\mathrm{GPS}} - \frac{1}{N_p(k)} \sum_{i=1}^{N_p(k)} \Delta\mathrm{PWV}_i^{\mathrm{InSAR}} + K \right\}^2, \quad (10)$$

where $N_{\mathrm{GPS}}$ is the number of GPS receivers, $N_p(k)$ is the number of InSAR pixels located within the circular area around the $k$th GPS receiver, $\Delta\mathrm{PWV}_k^{\mathrm{GPS}}$ is the temporal difference of PWV between master and slave dates by GPS, $\Delta\mathrm{PWV}_i^{\mathrm{InSAR}}$ represents the $\Delta$ PWV estimated by InSAR. Finally, the relative map of the $\Delta$ PWV from the interferograms were calibrated by subtracting the constant $K$ from the $\Delta\mathrm{PWV}^{\mathrm{InSAR}}$ map.

## 4   Results and discussion

In this section, we will evaluate and validate the performance of InSAR-based water vapour maps by comparing the calibrated $\Delta$ PWV estimated from InSAR to $\Delta$ PWV measurements from GPS, as well as measured values from MERIS. The evaluation was conducted as follows. PWV measurements at each GPS station were compared to PWV from MERIS. This comparison is important since possible errors in the GPS PWV can be detected by comparing them to MERIS PWV, a relatively high-accuracy retrieval of water vapour (Li et al., 2003). The calibrated $\Delta$ PWV maps of InSAR are compared to the absolute value of $\Delta$ PWV at each GPS station. This comparison helps to check the orbital errors due to the inaccurate satellite ephemeris and to verify that the unwrapped phase is only due to tropospheric delay and not to the Earth surface displacement. The last step is to compare the calibrated InSAR time series maps of $\Delta$ PWV to the MERIS water vapour maps on a pixel-wise basis. In such a way, it is possible to cross validate the accuracy of water
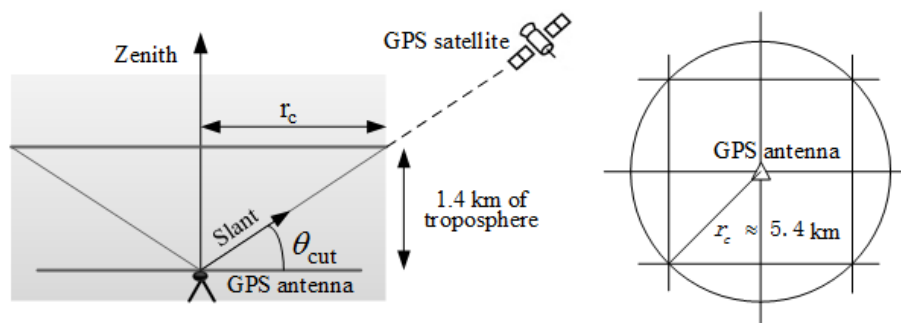
**Figure 5.** GPS receiver records a satellite signal at a cut-off elevation angle $\theta_{cut}$ defining a cone-like tropospheric section above the antenna. For $\theta_{cut} = 15°$, $r_c \approx 5.4$ km. The $\Delta$ PWV estimated by InSAR pixels within this circle are averaged to emulate GPS-based $\Delta$ PWV.
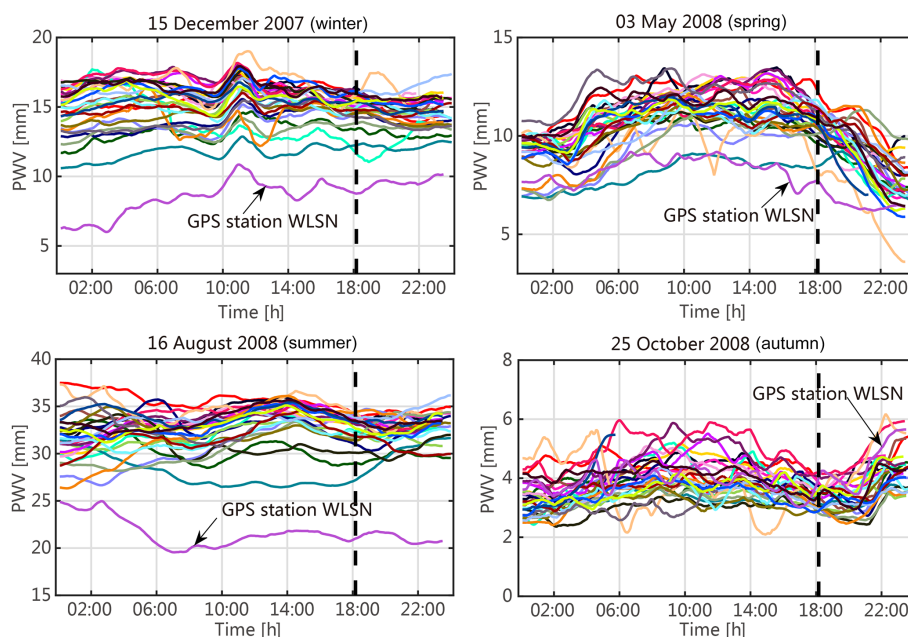


**Figure 6.** Time series over 24 h of PWV estimated from GPS observations at 29 GPS stations located in the study area (as shown in Fig. 1) on four SAR acquisition dates. The vertical black dashed lines represent the SAR satellite overpass time (18:01 UTC). Black arrows on each plot indicate the locations of GPS station WLSN (altitude about 1700) on Mount Wilson. In general, the higher the GPS station, the lower the PWV value.

vapour measurements and also inspect their spatial distribution properties.
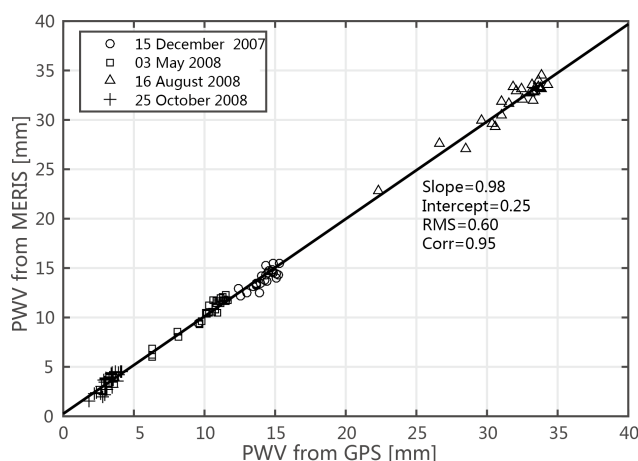
## 4.1 GPS PWV measurements

The tropospheric products analysed by CWU at the 29 GPS stations (Fig. 1) are used in this study. These products provide the zenith tropospheric delay at each GPS station every 5 min. The high temporal sampling of GPS measurements enables us to obtain the zenith wet delay at a time as close as possible to the SAR image acquisition time. The cut-off elevation angle ($\theta_{cut} = 15°$) was considered in the GPS data processing. The Saastamoinen model and gridded Vienna Mapping Function (VMF1GRID) (Kouba, 2007) were used for calculating a priori values of zenith hydrostatic delay. The

zenith wet delay was then obtained by subtracting the zenith hydrostatic delay from the total delay and the PWV was finally obtained by Eq. (6) using the water vapour conversion factor estimated from ERA-Interim reanalysis products.

As an example of the GPS PWV, Fig. 6 displays the 24 h time series of the PWV estimated from GPS observations at 29 stations on 15 December 2007 (winter), 3 May 2008 (spring), 16 August 2008 (summer) and 25 October 2008 (autumn), which are four of the SAR acquisition dates in our study. In summer, high temperature causes water to evaporate from the surfaces of lakes and oceans, resulting in higher and more variable PWV content, whereas in autumn and winter, a lower and smoother PWV was observed due to dry weather conditions.

**Table 1.** Acquisition dates of master and slave images and their parameter information.

| Number | Master (DDMMYYYY) | Slave (DDMMYYYY) | Normal baseline (m) | Temporal baseline (days) | Height ambiguity (m) |
|---|---|---|---|---|---|
| 1 | 6 October 2007 | 15 December 2007 | −62.75 | 70 | 146.83 |
| 2 | 6 October 2007 | 19 January 2008 | 36.16 | 105 | 254.84 |
| 3 | 15 December 2007 | 19 January 2008 | 98.34 | 35 | 93.77 |
| 4 | 19 January 2008 | 3 May 2008 | −51.85 | 105 | 177.05 |
| 5 | 3 May 2008 | 7 June 2008 | 217.11 | 35 | 42.54 |
| 6 | 3 May 2008 | 16 August 2008 | −191.01 | 105 | 48.30 |
| 7 | 7 June 2008 | 16 August 2008 | −27.67 | 70 | 333.19 |
| 8 | 16 August 2008 | 25 October 2008 | 31.72 | 70 | 290.90 |
| 9 | 16 August 2008 | 29 November 2008 | −4298.42 | 105 | 30.92 |
| 10 | 25 October 2008 | 29 November 2008 | −284.21 | 35 | 32.48 |



**Figure 7.** MERIS PWV against GPS PWV at 29 stations on 4 days of ENVISAT overpass time. The MERIS observations are averaged within circles of 5.4 km radius centred on the GPS station.

**Table 2.** Constants used for calculating atmospheric delay (Smith and Weintraub, 1953).

| Constant | Value |
|---|---|
| $R_d$ | $287.05 \, \mathrm{J \, kg^{-1} \, K^{-1}}$ |
| $R_v$ | $461.95 \, \mathrm{J \, kg^{-1} \, K^{-1}}$ |
| $g_0$ | $9.81 \, \mathrm{m \, s^{-2}}$ |
| $k_1$ | $0.776 \, \mathrm{K \, Pa^{-1}}$ |
| $k_2$ | $0.716 \, \mathrm{K \, Pa^{-1}}$ |
| $k_3$ | $3.75 \times 10^3 \, \mathrm{K^2 \, Pa^{-1}}$ |
| $\rho$ | $1000 \, \mathrm{kg \, m^{-3}}$ |

In Fig. 7, we plot PWV measurements derived from MERIS against PWV results estimated from GPS at 29 stations on the 4 SAR acquisition days (in Fig. 6). Since GPS PWV estimates represent average values over the reversed cone with a ∼ 5.4 km radius base, we averaged the PWV from MERIS within the circular area around the locations of

the GPS stations. The result shows a strong correlation (0.95) between GPS and MERIS. The mean absolute error (MAE) of the differences between the two data sets does not exceed 0.5 mm and the root mean square (rms) value is 0.60 mm. The slope of the line in Fig. 7 is 0.98. Similar comparison was performed and the MERIS was validated to be the most accurate tool to map PWV at high resolution and was in principle particularly useful for InSAR tropospheric delay mitigation (Cimini et al., 2012). Thus GPS and MERIS measurements of water vapour are in good agreement and we should not expect a perfect correlation between the two data sets because we averaged the conical effect of GPS with a circle and there is noise in both data sets.

### 4.2 InSAR Δ PWV measurements

The eight ENVISAT ASAR images are used for interferometric processing. The constraints for normal baseline (< 300 m) and temporal baseline (< 105 days) are used in order to minimize the effects of ground deformation and decorrelation noise. Table 1 summarizes the baseline information and the height ambiguity for all of the interferograms. The height ambiguity is defined as the altitude difference that generates an interferometric phase change of $2\pi$ after interferogram flattening. Errors in the external DEM used to remove the topographic contribution will propagate into the phase results. Small values of the height of ambiguity indicate that possible errors in the external DEM could generate only negligible phase artifacts. This ensures that interferometric phase is primarily related to atmospheric delay. We used the DORIS software (Kampes et al., 2003) for interferogram generations and the small baseline technique in StaMPS software (Hooper et al., 2007) for selecting phase stable points. Adaptive power spectrum filters have been applied to interferograms to reduce phase noise (Goldstein and Werner, 1998). All interferograms were multilooked by 40 looks in azimuth and 8 looks in range to enhance the coherence quality and improve the phase unwrapping accuracy. The multilook processing resulted in a reduction of the spa-

**Table 3.** Assessment of Δ PWV maps obtained by InSAR after calibration of offset using GPS (master image from 16 August 2008, slave image from 25 October 2008). For each GPS station, PWV differences from GPS between master and slave SAR acquisition times are computed and compared to the average values of InSAR estimates at pixels located within a circular area of 5.4 km around each GPS station. Differences are summarized in the last column. MAE and SD represent the mean absolute error and standard deviation.

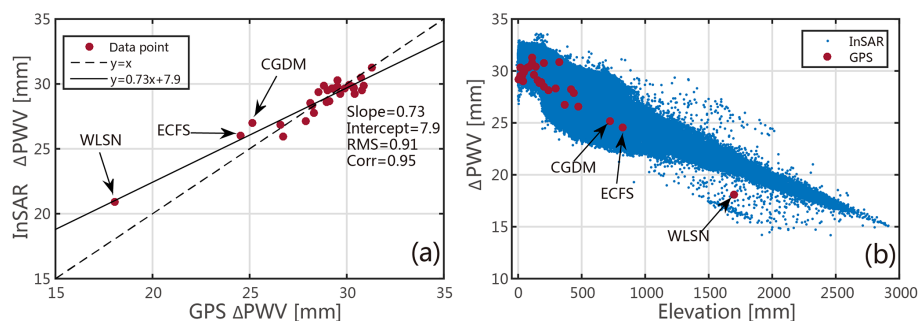| Number | GPS station | Longitude (°) | Latitude (°) | Δ PWV$_{GPS}$ (mm) | Δ PWV$_{InSAR}$ | | Difference (mm) |
| --- | --- | --- | --- | --- | --- | --- | --- |
| | | | | | Mean (mm) | SD (mm) | |
| 1 | AZU1 | −117.896 | 34.126 | 28.94 | 28.62 | 0.65 | 0.32 |
| 2 | BGIS | −118.159 | 33.967 | 30.15 | 29.92 | 0.47 | 0.23 |
| 3 | BKMS | −118.094 | 33.962 | 29.89 | 29.64 | 0.28 | 0.25 |
| 4 | CCCO | −118.211 | 33.876 | 29.50 | 30.26 | 0.43 | −0.76 |
| 5 | CGDM | −117.964 | 34.243 | 25.13 | 27.02 | 1.47 | −1.89 |
| 6 | CNPP | −117.608 | 33.857 | 30.87 | 29.84 | 1.37 | 1.03 |
| 7 | CVHS | −117.901 | 34.082 | 29.10 | 28.66 | 0.42 | 0.44 |
| 8 | DYHS | −118.125 | 33.937 | 29.03 | 29.50 | 0.30 | −0.47 |
| 9 | ECFS | −117.411 | 33.647 | 24.51 | 26.03 | 1.22 | −1.52 |
| 10 | EWPP | −117.525 | 34.104 | 26.71 | 25.98 | 0.46 | 0.73 |
| 11 | GVRS | −118.112 | 34.047 | 28.83 | 29.84 | 0.34 | −1.01 |
| 12 | HOLP | −118.168 | 33.924 | 29.53 | 29.77 | 0.50 | −0.24 |
| 13 | LBC1 | −118.137 | 33.832 | 30.29 | 29.78 | 0.32 | 0.51 |
| 14 | LBC2 | −118.173 | 33.791 | 29.31 | 29.68 | 0.32 | −0.37 |
| 15 | LBCH | −118.203 | 33.787 | 29.22 | 29.62 | 0.37 | −0.40 |
| 16 | LONG | −118.003 | 34.111 | 31.31 | 31.23 | 0.35 | 0.08 |
| 17 | LORS | −117.754 | 34.133 | 26.58 | 26.82 | 0.79 | −0.24 |
| 18 | MAT2 | −117.436 | 33.856 | 28.24 | 28.35 | 0.87 | −0.11 |
| 19 | NOCO | −117.569 | 33.919 | 30.77 | 29.51 | 0.90 | 1.26 |
| 20 | PSDM | −117.807 | 34.091 | 28.30 | 27.79 | 0.45 | 0.51 |
| 21 | RHCL | −118.026 | 34.019 | 28.53 | 29.36 | 0.64 | −0.83 |
| 22 | SBCC | −117.661 | 33.553 | 30.72 | 30.51 | 0.54 | 0.21 |
| 23 | SGDM | −117.861 | 34.205 | 27.87 | 27.15 | 1.16 | 0.72 |
| 24 | SPMS | −117.848 | 33.992 | 28.14 | 28.56 | 0.51 | −0.42 |
| 25 | VYAS | −117.992 | 34.030 | 30.39 | 29.24 | 0.52 | 1.15 |
| 26 | WCHS | −117.911 | 34.061 | 30.38 | 29.74 | 0.44 | 0.64 |
| 27 | WHC1 | −118.031 | 33.979 | 29.66 | 29.21 | 0.64 | 0.45 |
| 28 | WLSN | −118.055 | 34.226 | 18.08 | 20.92 | 1.61 | −2.84 |
| 29 | WNRA | −118.059 | 34.043 | 30.34 | 29.68 | 0.45 | 0.66 |
| MAE | | | | | | | 0.70 |
| SD | | | | | | | 0.96 |



**Figure 8. (a)** GPS Δ PWV plotted against the calibrated Δ PWV from the interferogram (master image from 16 August 2008, slave image from 25 October 2008). The slope of the solid line in the figure is 0.73, large differences were found on stations CGDM, ECFS and WLSN. **(b)** GPS (red) and InSAR (blue) Δ PWV plotted as a function of elevation. Black arrows indicate the locations of GPS sites CGDM, ECFS and WLSN.
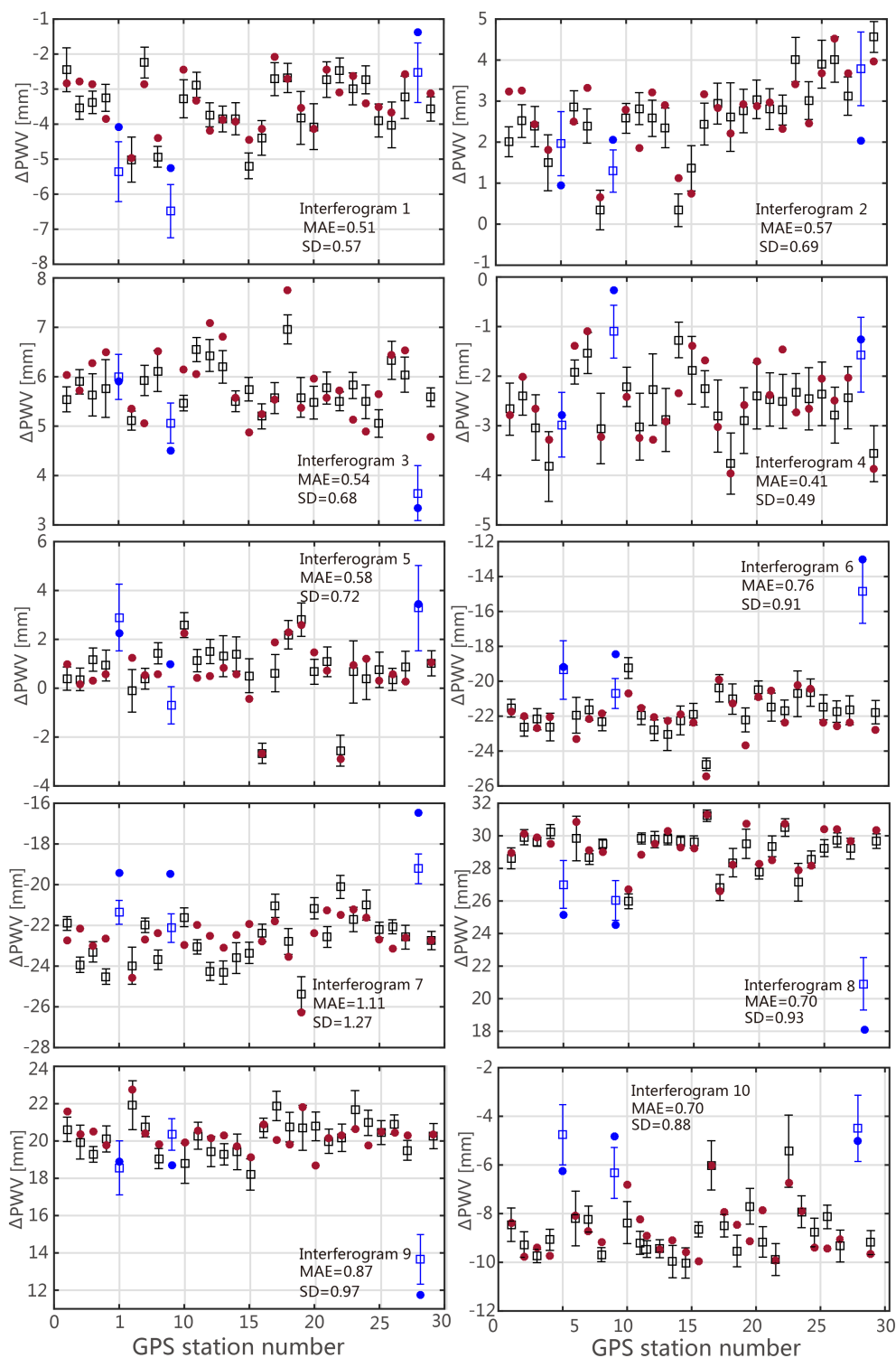
**Figure 9.** Comparisons of Δ PWV estimates from InSAR (squares) and collocated GPS measurements for each GPS station (circles). The InSAR Δ PWV is estimated from the 10 interferograms in Table 1. The squares indicate Δ PWV estimates from InSAR that are obtained by averaging all pixels falling within the circular area with a radius of 5.4 km centred around the station, corresponding to the observational cone above the GPS receiver. The error bars denote standard deviation of the pixel values in the circular area. The blue colour in each plot (from left to right) represents the GPS stations CGDM, ECFS and WLSN respectively.

**Figure 10.** Scatter plot of $\Delta$ PWV from GPS and InSAR. The data points (grey circles) are from Fig. 9.

tial resolution of the interferograms to $160\,\mathrm{m} \times 160\,\mathrm{m}$. The wrapped phases were unwrapped using a branch cut algorithm (Goldstein et al., 1988) and possible orbital errors were corrected by network de-ramping method. Oscillator drifts induce a systematic phase ramp in the interferogram from the ENVISAT satellite (Marinkovic and Larsen, 2015), they were removed by the script provided in the StaMPS software. The local rapid ground subsiding region was masked out. The wet delay differences of InSAR were obtained by subtracting the component of hydrostatic delay predicted from the ERA-Interim model. The wet delay differences were finally mapped onto $\Delta$ PWV maps using the water vapour conversion factor as explained in Sect. 3.2.

Due to the fact that the unwrapped processing introduced an arbitrary constant into the phase, all the $\Delta$ PWV maps from InSAR were relative measurements. Therefore, we need the calibration by using the ground measurements of PWV from GPS. The GPS PWV values were estimated from the zenith wet delay provided by the CWU data analysis centre as described in previous section. The overpass time of ENVISAT satellite was 18:01 UTC, thus we computed the temporal difference of the PWV at each GPS station at time 18:00 UTC, making the time differences negligible. Using the $\Delta$ PWV estimates from GPS, the $\Delta$ PWV maps of InSAR were calibrated by solving the cost function (Eq. 10) as described in Sect. 3.3. A comparison of the calibrated $\Delta$ PWV from the interferogram (master image from 16 August 2008, slave image from 25 October 2008, see Fig. 2) and $\Delta$ PWV from the 29 GPS stations is displayed in Fig. 8a. The slope of the line in this figure is 0.73 while the correlation coefficient is 0.95, suggesting the GPS and InSAR measurements of PWV are in reasonable agreement, although there is noise in both data sets. Figure 8b plots the $\Delta$ PWV from GPS and InSAR as a function of elevation. This plot shows that the content of water vapour is significantly dependent on the terrain height. The dependence on height of $\Delta$ PWV is roughly linear or better exponential as the concentration of water vapour

generally decreases linearly or exponentially with elevation (Basili et al., 2014). However, since we obtained the water vapour difference between two SAR acquisitions, it may happen that $\Delta$ PWV can decrease but also increase with height. The decreasing trend in Fig. 8b implies that the absolute water vapour content was smaller at the acquisition time of the slave image than at the acquisition time of the master image. The quantitative comparison of this interferogram is summarized in Table 3. It can be seen that most of differences are smaller than 2 mm. The MAE of $\Delta$ PWV between GPS and InSAR is 0.70 mm and the rms value is 0.91 mm. It is worth noting that large differences between InSAR and GPS at stations CGDM, ECFS and WLSN (indicated by the black arrows in Fig. 8) were observed, and the largest difference ($-2.84$ mm) was observed at station WLSN. The standard deviations of InSAR pixels located within the circular area around these three GPS stations also show a high value (the fourth column in Table 3). The three GPS stations are located in mountain areas with an altitude 730, 820, 1700 m for the CGDM, ECFS and WLSN stations respectively. This interferogram also shows a high value for height ambiguity (290.90 m). Therefore, we can conclude that the large discrepancies between InSAR and GPS for these three stations are most probably due to the topographic phase error during interferometric processing.

The comparisons of $\Delta$ PWV from the two techniques at each GPS station for the 10 interferograms are shown in Fig. 9. A good agreement between the InSAR and GPS was found across the whole data set. Large differences between InSAR and GPS at stations CGDM, ECFS and WLSN were also found on those interferograms with a high value of height ambiguity (interferograms 1, 2, 4 and 7 in Table 1). In Fig. 10, we put all the data points in a scatter plot. The rms difference of InSAR $\Delta$ PWV with respect to the GPS $\Delta$ PWV is better than 1 mm, and the correlation is 0.97. The PWV estimates from the two techniques are characterized by different sampling properties both in space and time. GPS can provide an absolute value of the PWV every 5 min but refers to the parts of atmosphere observed within a cone with a radius depending on the elevation cut-off angle, whereas InSAR gives a high-spatial-resolution map of the $\Delta$ PWV with a time separation of 35 days or more. The high temporal sampling of GPS and high spatial resolution of InSAR are complementary for numerical weather modelling, which will improve the model resolution and give a better understanding of the structure of atmospheric patterns.

## 4.3 Validation using water vapour measurements from MERIS

In this section, we will evaluate and analyse the accuracy of time series of the calibrated $\Delta$ PWV maps derived from InSAR to confirm the performance of this technique as a tool for constructing PWV maps. We carry out a cross-validation pixel by pixel using cloud-free water vapour pix-
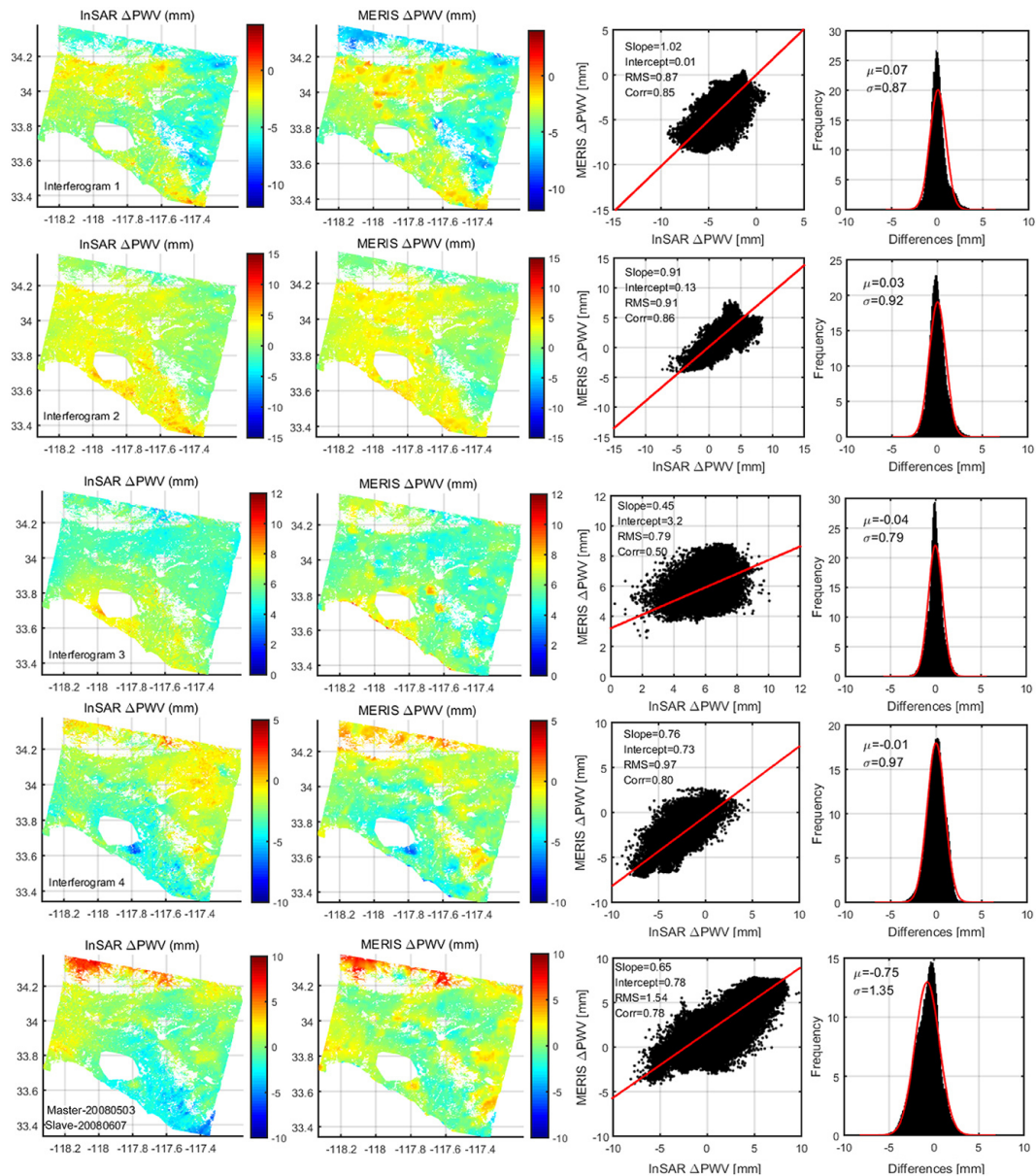
**Figure 11.**

els by MERIS acquired simultaneously with the ENVISAT ASAR images. The water vapour content is expressed as integrated water vapour (IWV) in the MERIS products. The theoretical accuracy of the MERIS IWV under cloud-free conditions over land is $0.16 \, \text{g m}^{-2}$ (Bennartz and Fischer, 2001) at full resolution ($\sim 300 \, \text{m}$), which corresponds to 1.6 mm accuracy in PWV. This accuracy will deteriorate under cloudy conditions or over water surfaces. The percentage of cloud-free conditions for MERIS data we used in this study are larger than 90 % except for the image acquired on 29 November 2008 having a coverage percentage of 80 %. For the sake of comparison, we built differences of PWV maps ($\Delta$ PWV) from MERIS. This is performed based on the software package called TRAIN (Toolbox for Reducing Atmospheric InSAR Noise) (Bekaert et al., 2015). Figure 11 shows the calibrated $\Delta$ PWV maps derived from the 10 interferograms (in Table 1) and the corresponding $\Delta$ PWV maps from MERIS data. The first column shows the $\Delta$ PWV derived from InSAR that has been calibrated with GPS observations. The $\Delta$ PWV from MERIS is shown in the second column. The third column shows the scatter plot of $\Delta$ PWV with InSAR on the abscissa and MERIS on the ordinate scale. The histogram of the frequency distributions of the differences between InSAR and MERIS are shown in the fourth column. For all images, the correlation coefficients (Corr) between InSAR and MERIS are computed as well as the root mean
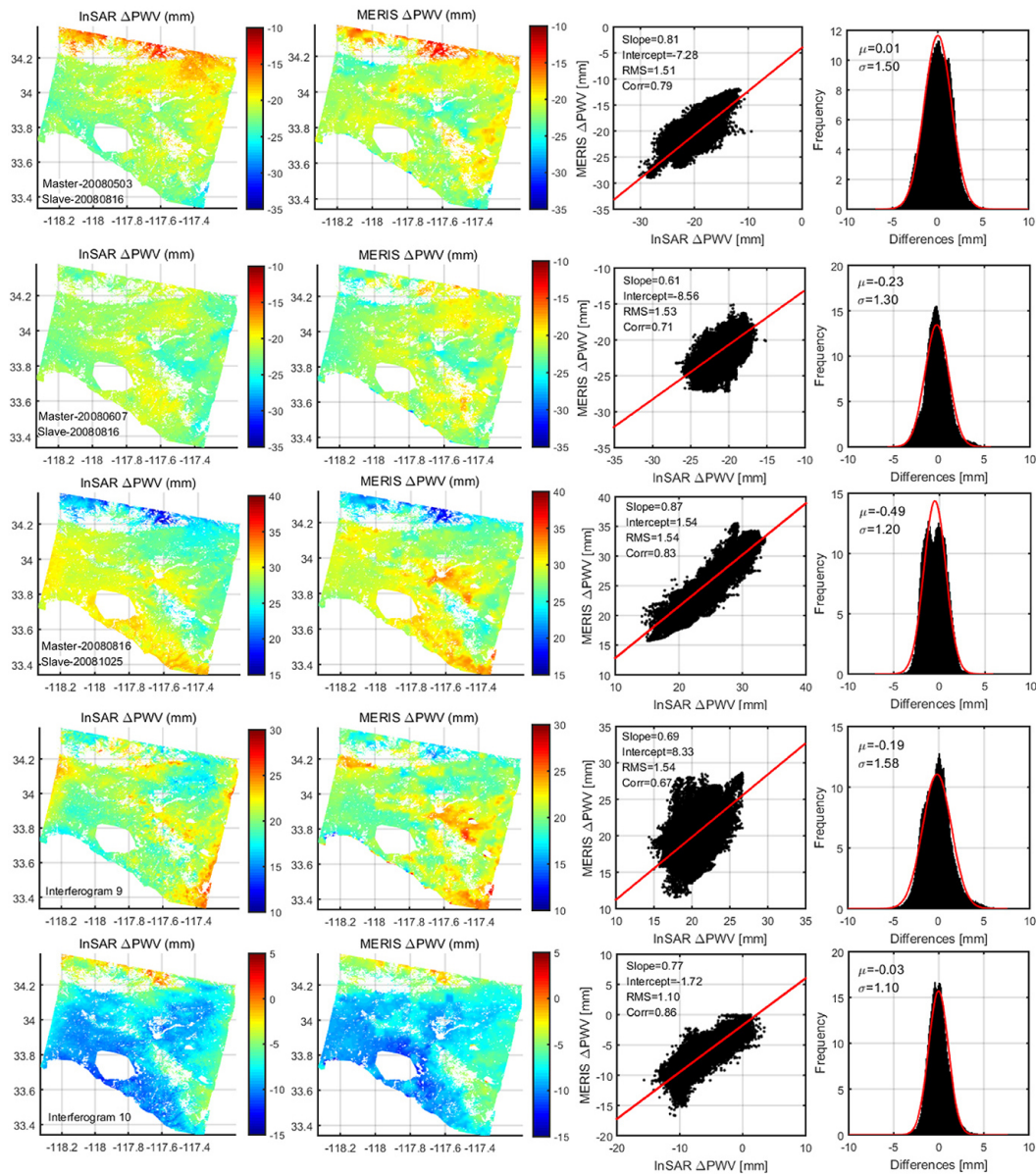
**Figure 11.** Comparison of the Δ PWV maps derived from InSAR and MERIS. For all images here, the root mean square (rms), correlation (Corr), differential mean (μ) and standard deviation (σ) are computed.

square (rms), mean (μ), and standard deviation (σ) of the differences between the two data sets. From visual comparison, InSAR Δ PWV and MERIS Δ PWV show a large spatial correspondence. Furthermore, the quantitative comparisons indicate high-correlation coefficients (Corr > 0.7) between the two data sets, except for interferogram 3 (master image from 15 December 2007, slave image from 19 January 2008) and interferogram 9 (master image from 16 August 2008, slave image from 29 November 2008) having correlation coefficients of Corr = 0.5 and Corr = 0.67 respectively. The differences between the InSAR and MERIS maps fol-

low a Gaussian distribution with mean values close to zero and standard deviations less than 2 mm.

## 5 Conclusion

In this paper, we presented the results of the temporal evolution of the PWV over southern California, USA using SAR interferograms during the period from 6 October 2007 to 29 November 2008. Interferograms were spatially averaged and spatial resolution was reduced to $160\,\text{m} \times 160\,\text{m}$. In order to improve the quality maps of atmospheric water vapour, the hydrostatic delay was precisely estimated by using ERA-

Interim reanalysis products. We also used the outputs from the ERA-Interim model to produce maps of the conversion factor for mapping zenith wet delay onto PWV at each pixel in the radar scene. All maps of $\Delta$ PWV derived from interferograms were calibrated using a network of 29 continuous GPS stations located in the SAR scene. The PWV estimates from InSAR and MERIS show strong agreement with the data from GPS. Since the GPS PWV estimates represent the average of the tropospheric effect within a cone above the receiver, InSAR and MERIS pixels were aggregated to enable a proper comparison. The comparative analysis between InSAR and MERIS $\Delta$ PWV maps demonstrates strong spatial correlation with a less than 2 mm standard deviation of difference. Our study demonstrates that satellite synthetic aperture radar interferometry can be applied to study the spatial distribution of the PWV with a spatial resolution of 160 m and an accuracy of $\sim$ 2 mm. This advantage of InSAR provides unsurpassed insights for capturing the small-scale water vapour distribution. This property could be important for numerical weather forecasting models. Furthermore, forecasting models could take advantage of this source of water vapour maps to enhance the accuracy of their assimilation systems. In turn, the more accurate atmospheric prediction models are beneficial for correcting the tropospheric delay affected by water vapour in the applications of geodesy.

## 6   Data availability

The ENIVISAT ASAR datasets were provided by ESA through Dragon-3 project (id10569). The GPS tropospheric products are archived at the UNAVCO Data Center (2016) and are openly and freely available at http://www.unavco.org/data/data.html. The 30 m SRTM DEM were downloaded from USGS EarthExplorer (2016) (http://earthexplorer.usgs.gov/). The ERA-Interim reanalysis came from the website of ECMWF (2016) (http://www.ecmwf.int/en/research/climate-reanalysis/era-interim).

## References

Basili, P., Bonafoni, S., Ciotti, P., and Pierdicca, N.: Modeling and Sensing the Vertical Structure of the Atmospheric Path Delay by Microwave Radiometry to Correct SAR Interferograms, IEEE T. Geosci. Remote, 52, 1324–1335, 2014.

Beauducel, F., Briole, P., and Froger, J.-L.: Volcano-wide fringes in ERS synthetic aperture radar interferograms of Etna (1992–1998): Deformation or tropospheric effect?, J. Geophys. Res., 105, 16391–16402, 2000.

Bekaert, D. P. S., Walters, R. J., Wright, T. J., Hooper, A. J., and Parker, D. J.: Statistical comparison of InSAR tropospheric correction techniques, Remote Sens. Environ., 170, 40–47, 2015.

Bennartz, R. and Fischer, J.: Retrieval of columnar water vapour over land from backscattered solar radiation using the Medium Resolution Imaging Spectrometer, Remote Sens. Environ., 78, 274–283, 2001.

Bevis, M., Businger, S., Herring, T. A., Rocken, C., Anthes, R. A., and Ware, R. H.: GPS meteorology : Remote sensing of atmospheric water vapor using the global positioning system, J. Geophys. Res., 97, 15787–15801, 1992.

Bevis, M., Businger, S., Chiswell, S., Herring, T. A., Anthes, R. A., Rocken, C., and Ware, R. H.: GPS meteorology: Mapping zenith wet delays onto precipitable water, J. Appl. Meteorol., 33, 379–386, 1994.

Cimini, D., Pierdicca, N., Pichelli, E., Ferretti, R., Mattioli, V., Bonafoni, S., Montopoli, M., and Perissin, D.: On the accuracy of integrated water vapor observations and the potential for mitigating electromagnetic path delay error in InSAR, Atmos. Meas. Tech., 5, 1015–1030, doi:10.5194/amt-5-1015-2012, 2012.

Davis, J. L., Herring, T. A., Shapiro, I. I., Rogers, A. E. E., and Elgered, G.: Geodesy by radio interferometry: Effects of atmospheric modeling errors on estimates of baseline length, Radio Sci., 20, 1593–1607, 1985.

Dee, D. P., Uppala, S. M., Simmons, A. J., Berrisford, P., Poli, P., Kobayashi, S., Andrae, U., Balmaseda, M. A., Balsamo, G., Bauer, P., Bechtold, P., Beljaars, A. C. M., van de Berg, L., Bidlot, J., Bormann, N., Delsol, C., Dragani, R., Fuentes, M., Geer, A. J., Haimberger, L., Healy, S. B., Hersbach, H., Hólm, E. V., Isaksen, L., Kållberg, P., Köhler, M., Matricardi, M., McNally, A. P., Monge-Sanz, B. M., Morcrette, J. J., Park, B. K., Peubey, C., de Rosnay, P., Tavolato, C., Thépaut, J. N., and Vitart, F.: The ERA-Interim reanalysis: configuration and performance of the data assimilation system, Q. J. Roy. Meteor. Soc., 137, 553–597, 2011.

Doin, M. P., Lasserre, C., Peltzer, G., Cavalié, O., and Doubre, C.: Corrections of stratified tropospheric delays in SAR interferometry: Validation with global atmospheric models, J. Appl. Geophys., 69, 35–50, 2009.

ECMWF: ERA-Interim reanalysis, available at: http://www.ecmwf.int/en/research/climate-reanalysis/era-interim, last access: 8 September 2016.

Farr, T. G., Rosen, P. A., Caro, E., Crippen, R., Duren, R., Hensley, S., Kobrick, M., Paller, M., Rodriguez, E., Roth, L., Seal, D., Shaffer, S., Shimada, J., Umland, J., Werner, M., Oskin, M., Burbank, D., and Alsdorf, D.: The Shuttle Radar Topography Mission, Rev. Geophys., 45, doi:10.1029/2005RG000183, 2007.

Goldstein, R. M. and Werner, C. L.: Radar interferogram filtering for geophysical applications, Geophys. Res. Lett., 25, 4035–4038, 1998.

Goldstein, R. M., Zebker, H. A., and Werner, C. L.: Satellite radar interferometry: Two-dimensional phase unwrapping, Radio Sci., 23, 713–720, 1988.

Hanssen, R.: "Radar interferometry", in: Data Interpretation and Error Analysis, Delft Univ. Technol., Delft, the Netherlands, 2001.

Hooper, A., Segall, P., and Zebker, H.: Persistent scatterer interferometric synthetic aperture radar for crustal deformation analysis, with application to Volcán Alcedo, Galápagos, J. Geophys. Res., 112, doi:10.1029/2006JB004763, 2007.

Jolivet, R., Grandin, R., Lasserre, C., Doin, M. P., and Peltzer, G.: Systematic InSAR tropospheric phase delay corrections from global meteorological reanalysis data, Geophys. Res. Lett., 38, doi:10.1029/2011GL048757, 2011.

Jolivet, R., Agram, P. S., Lin, N. Y., Simons, M., Doin, M.-P., Peltzer, G., and Li, Z.: Improving InSAR geodesy using Global Atmospheric Models, J. Geophys. Res.-Sol. Ea., 119, 2324–2341, 2014.

Kampes, B. M., Hanssen, R. F., and Perski, Z.: Radar interferometry with public domain tools, Frascati, Italy, 1–5, 2003.

Kouba, J.: Implementation and testing of the gridded Vienna Mapping Function 1 (VMF1), J. Geodesy, 82, 193–205, 2007.

Li, Z. H., Muller, J. P., and Cross, P.: Comparison of precipitable water vapor derived from radiosonde, GPS, and Moderate-Resolution Imaging Spectroradiometer measurements, J. Geophys. Res., 108, doi:10.1029/2003JD003372, 2003.

Liao, M., Jiang, H., Wang, Y., Wang, T., and Zhang, L.: Improved topographic mapping through high-resolution SAR interferometry with atmospheric effect removal, ISPRS J. Photogramm., 80, 72–79, 2013.

Marinkovic, P. and Larsen, Y.: On resolving the local oscillator drift induced phase ramps in ASAR and ERS1/2 interferometric data – the final solution, Fringe 2015 workshop, 23–27 March 2015, Frascati, Italy, 318, 2015.

Mateus, P., Nico, G., and Catalão, J.: Can spaceborne SAR interferometry be used to study the temporal evolution of PWV?, Atmos. Res., 119, 70–80, 2013a.

Mateus, P., Nico, G., Tome, R., Catalao, J., and Miranda, P. M. A.: Experimental study on the atmospheric delay based on GPS, SAR interferometry, and numerical weather model data, IEEE T. Geosci. Remote, 51, 6–11, 2013b.

UNAVCO Data Center: GPS tropospheric products, available at: http://www.unavco.org/data/data.html, last access: 8 September 2016.

USGS EarthExplorer: SRTM DEM, available at: http://earthexplorer.usgs.gov/, last access: 8 September 2016.

Smith, E. K. and Weintraub, S.: The constants in the equation for atmospheric refractive index at radio frequencies, Proceedings of the IRE, 41, 1035–1037, 1953.

Zebker, H. A., Rosen, P. A., and Hensley, S.: Atmospheric effects in interferometric synthetic aperture radar surface deformation and topographic maps, J. Geophys. Res., 102, 7547–7563, 1997.